Identification of magnetic enhancement at hydrocarbon/water contacts.

Badejo, S. A.,[1] Muxworthy, A. R.,[1] Fraser, A.,[1] Stevenson, G. R.,[1] Zhao, X.[2] and Jackson, M.[3]

[1] Department of Earth Science and Engineering, Imperial College London, London.

[2.] Research School of Earth Sciences, Australian National University, Canberra, ACT, Australia

[3.]Institute for Rock Magnetism, University of Minnesota, Minneapolis, Minnesota, USA

Abstract

Identifying the depths of the hydrocarbon-fluid contacts in a reservoir is important for determining hydrocarbon reserves and production planning. Using core samples from the Tay sandstone reservoir in the Central North Sea, we show that there is a magnetic enhancement at the hydrocarbon-fluid contacts, that is detectable both through magnetic susceptibility measurements and magnetic hysteresis measurements. We observed this magnetic enhancement at both gas-oil and oil-water contacts, that have been independently identified using non-magnetic methods; we did not consider gas-water contacts in this study. We demonstrate that this magnetic enhancement is due to the precipitation of new nanometric iron oxide (magnetite) and iron sulphide (greigite) phases. The magnetic enhancement may be caused by diagenetic changes or preferential biodegradation at the top of the oil column during early filling and at the oil water contact. Our findings have the potential to be used to identify paleo-hydrocarbon-fluid contact in both structurally modified fields and failed wells. The technique can also be used to infer the fill history of a basin and calibrate petroleum systems models. Magnetic susceptibility measurements have the advantage that they can easily and quickly be measured in the field on whole core-material.

1. Introduction

Hydrocarbon fluid contacts are boundaries that separate hydrocarbon phases from each other and from the formation water (Ahmed, 1989). Identifying the locations of these hydrocarbon fluid contacts is crucial for determining hydrocarbon reserves and production planning.

As source rocks undergo burial, oil is generated and then expelled. The oil usually migrates upwards due to buoyancy, until it escapes at the surface/seabed or is trapped in a reservoir. As burial depth increases, depending on the kerogen type, the source rock can also expel gas which also migrates upwards but typically at faster rates than oil. If gas reaches the reservoir it will dissolve in the oil, potentially creating a multi-phase system depending on pressure and temperature (Larter and di Primio, 2005). As pressure drops or temperature increases, the gas exsolves from the oil and a gas cap is formed above the oil with the formation water lying below the oil (Ahmed, 1989).

Resistivity wireline logs (Fig. 1) are good for identifying oil-water contacts (OWC) and gas-water contacts (GWC), as the resistivity of hydrocarbons is significantly higher than that of water (Rider and Kennedy, 1996). However, as oil and gas have roughly the same resistance, resistivity logs cannot be used to differentiate gas-oil contacts (GOC). To identify GOC (and GWC) contacts, neutron porosity and density wireline logs can be used; gas is less dense than oil or water, and because neutron-derived porosities for gas are significantly under-estimated this provides a clear contrast (known as the “gas effect”) as shown in Fig. 1 (Rider and Kennedy, 1996). It has been found that hydrocarbon fluid contacts are not always sharp boundaries; they can be gradational with an intermediate transition zone of mixed fluids. Depending on the lateral pressure variation in the reservoir bed can be flat or tilted (Dennis et al., 2000). If pressure data (e.g. wireline repeat formation tester (RFT) data) are available an accurate determination of fluid contacts can be made.

The reducing conditions generated by hydrocarbons can alter (produce or destroy) the ferromagnetic minerals that may be present, that is, iron oxides and iron sulphides depending on the conditions (Reynolds et al., 1990; Emmerton et al., 2012; Abubakar et al., 2015; 2020). The iron oxide magnetite, and the iron sulphides pyrrhotite and greigite, are the most common magnetic minerals precipitated, while the iron oxide hematite, if initially present, typically gets replaced or dissolved. Also common in these environments are iron-rich non-magnetic minerals such as pyrite and siderite

(Machel, 1995). The exact balance of magnetic and non-magnetic iron-rich minerals depends on the local environment.

Mineral magnetic measurements carried out on shallow drill cuttings from oil-producing and dry wells from oil fields in Venezuela, have found magnetic susceptibility anomalies in oil-producing wells that are due to the presence of Fe-rich spherical aggregates and magnetic phases of authigenic origin (Costanzo-Alvarez et al., 2000; Aldana et al., 2003). Similarly, Liu et al. (2006) found that in addition to anomalies in the magnetic susceptibility, magnetic hysteresis parameters that are mass dependent, e.g., saturation magnetisation and remanent saturation magnetisation, were 2 - 5 times higher in oil producing zones compared to non-oil producing zones with fine grained (~ 25 nm) magnetite contributing to this enhanced signal. This enhanced signal in the oil-bearing layers has also been attributed to the presence of fine grained pyrrhotite in oil wells located in Venezuela and Oklahoma, USA (Reynolds et al., 1990; Mena and Walther, 2012).

We have identified a magnetic enhancement at hydrocarbon-fluid contacts. In this paper we show that peaks in magnetic susceptibility, saturation magnetisation and remanent saturation, coupled with size of magnetic minerals, can be used to determine the hydrocarbon contacts on core samples. These new approaches have the potential to be used in the identification of paleo-hydrocarbon-fluid contacts, which are vital to understanding the fill history of basins. To demonstrate these effects, we have obtained and studied core samples from the Tay formation in the Central North Sea Basin.

2. **Study Area**

The wells used in this study are in the Central North Sea (CNS) Basin of the UK North Sea (Fig. 2). The Central Graben is located about 240 km east of Scotland and is one of the three arms of the failed North Sea rift system which also includes the Viking Graben and the Inner and Outer Moray Firth (Erratt et al., 1999).

A stratigraphic column of the study area is shown in Figure 3. The Upper Jurassic Kimmeridge Clay is the main source rock in the area (Fig. 3). It is mature for oil to the east of the study area with burial depths greater than 3250m and generally late mature for oil to early mature for gas at the eastern

edge with burial depths of about 4750m (Isaksen, 2004). In the Central Graben the main hydrocarbon reservoirs are Upper Jurassic shallow marine sandstones and Tertiary deep-water sandstones.

Initial accumulation of oil was in the Upper Jurassic Fulmar sandstones. As the source rock lies directly above this formation it makes an ideal short distance migration pathway. However, the Fulmar is affected by both stratigraphic complexity and salt movement which makes sandstones often discontinuous and fractured. Over time sediment loading led to capillary failure in the seal above the Fulmar sandstones, which initiated vertical migration, with the fractured chalk and possibly the salt wall and diapirs acting as a vertical conduits for migration into the overlying Tertiary sandstones. In our study area, 3D basin modelling (Badejo et al., 2020) suggests the oil migrates vertically to the Tay sandstone member of Eocene age in the east and moves laterally to the west by a fill and spill mechanism. All the core samples studied are from this formation.

Compared to the Fulmar sandstones the Tertiary sandstones are only slightly deformed and laterally continuous, facilitating lateral migration of distances of up to 50km for oil and up to 32km for gas (Cayley, 1987; Kubala et al., 2003).

3. Methodology

3.1 Sample collection

Well cores were sampled from the British Geological Survey core repository in Keyworth, UK. Composite logs were used to determine which wells in the study area have penetrated OWCs or GOCs or both: 6 out of the 18 wells selected have core material with a clear OWC, while only 2 wells sample a clear GOCs. The composite logs were also used to determine the presence of hydrocarbon is in the Tay formation and if the core recovery was successful from the formation. Samples were selected based on geological observation (water wet sandstone, oil stained sandstone, sandstones in gas cap, siltstones and shale). Samples taken were typically 2cm chips. Data from wells 21/25-04, 21/25-A1 and 21/29a-08 are shown in this paper.

In addition to the core sections, pure oil samples were obtained from wells 21/29a-8 and the 21/24-2 (Fig. 2). The oil samples were absorbed in kaolinite clay for magnetic measurements. To purify the kaolinite clay, it was washed in hydrogen peroxide to get rid of any organic matter, then it was washed

in deionised water and left in an oven at 100°C for 24 hours. For each sample the mass of the kaolinite clay was measured before (1.98 g per sample) and after oil was added (about 3 g). Approximately, 0.15g of the mixture was used for the Low temperature (LT) experiments. The concentration of oil in both samples was ~ 35% by total mass; we subtracted that from the overall signal.

3.2 Magnetic Measurements

Magnetic measurements were carried out to determine the morphology, mineralogy and size of the magnetic minerals present. The magnetic techniques used are described below.

3.2.1 Magnetic Hysteresis Measurements

Room-temperature magnetic-hysteresis measurements on a vibrating sample magnetometer (VSM) were done in Imperial College London. The VSM measures the magnetic response to an applied field. All materials fall into one of the three magnetic categories: diamagnetic, paramagnetic or ferromagnetic. Diamagnetic and paramagnetic minerals have a linear relationship with the applied field, with negative and positive slopes, respectively (Dunlop and Özdemir, 1997). In ferromagnetic materials, the magnetisation does not return to zero when the field is removed but retains a record of the applied field. The path of magnetisation as a function of the applied field is known as a hysteresis loop. If the applied field reaches a sufficient level, the material acquires its saturation magnetisation (M_s). Removing this field gives a remanent saturation magnetisation (M_{rs}). To reduce the magnetisation to zero a reverse field, coercive force (H_c) is applied.

In very small grains, the magnetisation is uniform, and the particle is said to be single domain (SD) (Dunlop and Özdemir, 1997). As a grain gets bigger its magnetisation breaks up into areas (domains) of uniform magnetisation separated by narrow domain walls; such grains are termed multidomain (MD). Small SD grains have magnetic moments that are unstable due to thermal fluctuations (< 30 nm for magnetite), and are called superparamagnetic (SP) grains or thermally relaxing SD grains (Dunlop and Özdemir, 1997). Small MD grains just above the SD/MD threshold size (~100 nm for

magnetite), display SD-like characteristics and are termed pseudo-single domain grain (PSD) (Roberts et al., 2017).

First-order reversal curves (FORC) diagrams are used to identify the domain state distributions within a sample (Roberts et al., 2000; Roberts et al., 2014). A FORC diagram is calculated from a class of partial hysteresis curves (Roberts et al., 2000). As a first approximation the x-axis represents the coercivity while the y-axis describes the magnetic interaction within the sample. The 'irregular' measurement protocol by Zhao et al. (2015) was used for all the FORCs in this paper.

3.2.2 Low-temperature measurements.

Low-temperature (LT, 20 – 300 K) experiments were carried out on the Magnetic Properties Measurement System (MPMS) at the University of Minnesota's Institute for Rock Magnetism in Minneapolis. These measurements assist identification of the magnetic minerals present based on mineral-specific crystallographic transitions, e.g., the Verwey transition in magnetite at T_V~120 K (Verwey, 1939), the Morin transition in hematite at T_M~263 K (Morin, 1950), the Besnus transition in monoclinic pyrrhotite at T_{Bes}~ 30-34 K (Besnus and Meyer, 1964), and to identify nanometric particles (< 30 nm) that are difficult to detect at room-temperature due to high thermal energy.

3.2.3 Susceptibility Measurements

High-temperature (HT) experiments were carried out on a KLY-2 KappaBridge AC Susceptibility Bridge in Imperial College London. Susceptibility was measured as samples were heated from room temperature to 700 ^{o}C in an argon atmosphere. This is used to help determine the mineralogy of the samples based on their Curie temperature and thermomagnetic behaviour (Dunlop and Özdemir, 1997).

A Variable Field Susceptibility Meter (VFSM) was used to measure the magnetic susceptibility at room temperature over a wide range of frequencies (30 Hz – 10 kHz) at a field of 300 Am^{-1} at Imperial College London. For small grains, susceptibility varies as a function of frequency because the grains behave as SP grains at low frequency and behave as SD grains at high frequency; larger grains, i.e., > 40 nm are essentially invariant to the applied frequencies (Muxworthy, 2001).

3.2.4 Scanning electron microscopy

As the abundance of magnetic minerals was less than 1% of the sample, magnetic extraction was needed for imaging. Samples were crushed to an even grain size, and a passed through a Frantz electromagnet magnetic separator 3 times to reduce the abundance of non- magnetic materials.

Samples were grounded and coated in gold for imaging energy dispersive X-ray (EDX) analysis on the Zeiss LEO Gemini 1525 scanning electron microscope (SEM) at Imperial College London. EDX analysis had a spot size of about 1 μm. Some uncoated samples were also imaged on a Phenom desktop SEM.

4. Results

4.1 Oil Samples

The following low-temperature experiments were carried out on the samples to identify possible magnetic transitions: (1) Low-temperature demagnetisation: the samples were induced with a SIRM at room-temperature (RTSIRM; field = 2.5 T), and then cooled to 10K and back to 300 K in zero-field. This generates two curves called RTSIRM cooling and RTSIRM warming curves; (2) Field cooled (FC) – Zero-field cooled (ZFC) warming curves: Induce a SIRM at 10 K and warm in zero field to 300 K. In the ZFC scenario the sample is first cooled to 10 K in zero field, in the FC scenario in a field a 2.5 T. RTSIRM cooling/warming and FC/ZFC curves were measured for the blank kaolinite clay, and for the oil from wells 21/24-02 and 21/29a-08 (Fig. 4). The curves for the blank kaolinite clay (Fig. 4 a) are noisy and show no evidence for any magnetic minerals. In comparison, the signal-to-noise ratio for the oil samples (Fig. 4b-c) is much higher, i.e., magnetisation is about two orders of magnitude stronger.

Drops in remanence at around 120 K on the RTSIRM cooling curve suggest the presence of magnetite in both wells (Fig. 4b-c), while a drop in magnetisation at around 37 K on the cycling cooling curve (Fig. 4b) could be due to the presence of monoclinic pyrrhotite in well 21/24-02 (Verwey, 1939; Besnus and Meyer, 1964).

4.2 Core Samples

Hysteresis loops (Fig. 5), FORC diagrams (measured if signal/noise ratio in the loop was high enough) and susceptibility were measured for all samples. An increase in M_s, M_{rs} and susceptibility

184 (normalised by mass) were noticed at the hydrocarbon fluid contacts as shown in wells 21/25-04,
185 21/25-A1and 21/29a-08 (Fig. 6). Differences in susceptibility measured at 990 Hz and 6000 Hz
186 observed in samples from well 21/25-A1 and 21/25-04 (Fig. 6d and e) suggest the presence of SP
187 grains, i.e., 25-35 nm in size (Muxworthy, 2001; Mena and Walther, 2012).

188 The LT experiments identified the presence of magnetite (decrease in remanence at about 120 K) in
189 all the samples (Fig. 7 and Fig. 8). The increase in remanence on cooling noticed in most of the
190 samples e.g. s63594, s63600, s73397 and s72399 (Figs. 7a and m and Figs. 8 d and g respectively)
191 suggests the presence of goethite or titanohematite (Sprain et al., 2016). RT-SIRM cooling and
192 warming curves identified the presence of hematite (drop in remanence at about 250 K) in a few
193 samples e.g. s63599 (Fig. 7j). This was expected as hematite is often replaced or dissolved in
194 diagenetic settings caused by hydrocarbons (Burton et al., 1993).

195 No Besnus transition was noticed in any of the LT curves measured, indicating there is no monoclinic
196 pyrrhotite in the samples, but other iron sulphides such as hexagonal pyrrhotite or greigite may be
197 present as they have no low temperature transition (Horng, 2018). The absence of a lambda
198 transition (rapid increase in susceptibility at ~200 ^{0}C followed by a rapid decrease in susceptibility at
199 250 ^{0}C) in the HT-susceptibility experiments suggests a lack of hexagonal pyrrhotite in the samples
200 (Dunlop and Özdemir, 1997). Greigite is typically unstable during heating with thermal decomposition
201 from 200- 400 ^{0}C (Chang et al., 2008). Its presence in samples is inferred from the HT-susceptibility
202 heating and cooling behaviours; kinks in susceptibility on heating between 200 and 400 ^{o}C e.g.
203 s72399, s7203 and s72406 (Figs. 8h, k and n respectively) have been attributed to the presence of
204 greigite (Dekkers et al., 2000).

205 Siderite is paramagnetic at room temperature, but in the presence of a field it acquires a large thermal
206 remanence on cooling below its Néel temperature (~37 K) (Frederichs et al., 2003). On heating of
207 low-temperature SIRM after FC or ZFC, there is a noticeable drop in remanence between 10 and 40
208 K in the FC experiment. This was used to identify the presence of siderite as shown in samples
209 s63599 and s72399 (Fig. 7j and Fig. 8g). In the absence of FC and ZFC curves, the heating and
210 cooling behaviour of susceptibility was used to identify siderite. When heating in argon siderite alters
211 to magnetite above 400 ^{o}C and on cooling a rapid increase in susceptibility at 580^{o}C accompanied

by a Hopkinson like peak is observed suggesting the formation of SP magnetite (Housen et al., 1996). This behaviour was noticed in samples s63594, s63596, s63598, s63599, s63600, s72396, s72397, s72399 and s72403 (Figs. 7b, e, h, k, n and Figs. 8b, e, h and k).

FORC diagrams with a vertical spread of concentric contoured peaks on the B_i=0 axis suggest the presence of interacting SD particles (Roberts et al., 2000). Such behaviour is observed at the hydrocarbon fluid contacts seen in s63594, s63599 (Fig. 7f and i). FORC diagrams with a contoured peak below the B_i=0 axis are indicative of SD greigite (Horng, 2018); this was observed in one well 21/25-A1 at the OWC (sample s72403; Fig. 8l). FORC diagrams for some samples have a vertical spread on the B_i axis, which suggest the presence of PSD grains (Roberts et al., 2000; Roberts et al., 2017) as seen in s63594, s63596 and s63598 (Figs. 7 c, f and i). FORC diagrams also suggest the presence of SP grains (Roberts et al., 2018) above and below the hydrocarbon fluid contact as seen in samples s63594, s63598, s63600, s72396, s72399 and s72406 (Figs. 7c, i and o and Figs. 8c, i and o). Samples with multiaxial anisotropy were identified by the steeply dipping negative region to the right of the B_u axis (Valdez-Grijalva and Muxworthy, 2019) (Figs. 7c, f and i and Fig. 8c, f, i, l and o). This feature may also be due to SD vortex behaviour (Lascu et al., 2018; Valdez-Grijalva et al., 2018).

SEM images on magnetic extracts showed a variety of grain sizes and iron-phase mineralogy. Framboids were found in samples such as s63598 (Fig. 9a). EDX analysis of the framboid in Fig. 9, identified iron- and sulphur-containing grains, which are likely (the EDX was not calibrated for this) a mixture of 1-2 μm sized pyrite grains and smaller < 100 nm greigite grains. Bigger magnetite and pyrite grains (3-5 μm sized) were found as well, e.g., s63597 (Fig. 9b); the bigger magnetite grains are likely responsible for the PSD behaviour noticed in s63594, s63596 and s63598 (Fig. 7c, f and i). EDX confirmed the presence of iron oxide minerals, which are most likely magnetite grains ranging from 50-350 nm in size (Fig. 9c-d).

5. Discussion

Peaks in saturation magnetisation, remanent saturation magnetisation and susceptibility have been found at the hydrocarbon fluid contacts (Fig. 6). The hysteresis parameters have been 'slope corrected', i.e., linear diamagnetic and paramagnetic contributions removed, however, the

susceptibility measures the total magnetic signal, which possibly includes contributions from Fe-bearing paramagnetic minerals which are common in, for example, clays. The behaviour at the OWC appears clear, there is an enhancement in both the hysteresis (ferromagnetic) signal and the susceptibility (ferromagnetic and paramagnetic). At the GOC there is an enhancement in the ferromagnetic signal, but in Fig. 6d, it is seen that the combined paramagnetic and ferromagnetic signal is invariant to the GOC. We suggest that the ferromagnetic minerals at this GOC are forming at the expense of the paramagnetic signal, i.e., Fe-rich paramagnetic minerals are becoming ferromagnetic.

FORC diagrams from samples at the hydrocarbon fluid contacts (Figs. 7f and l and Fig. 8l respectively) suggest the presence of stable SD grains, i.e., ~50-100 nm. FORC diagrams from samples above and below the hydrocarbon contacts suggest the presence of smaller SP grains and PSD grains (Figs. 7c, i and o and Figs. 8c, i and o). LT and HT experiments confirmed the presence of magnetite, greigite, siderite, hematite, titanohematite and goethite in the samples (Figs. 7 and 8). Only magnetite was observed in the oil-well samples, with possibly monoclinic pyrrhotite also present.

5.1 Can magnetic minerals be carried in the oil?

The oil samples from wells 21/24-02 and 21/29a-08 (Fig. 5b-c) have magnetisations that are two orders of magnitude higher than the kaolinite clay sample (Fig. 5a) and contain magnetite (identified by its Verwey transition at ~ 120 K). This suggests the magnetic minerals can form complexes within the oil that can be transported from the source rock to the reservoir provided they are small enough to fit through the pore throats of the carrier beds. The presence of framboids, e.g., s63597 (Fig. 9a), suggests the diagenetic conditions caused by the oil could lead to the precipitation of magnetic and non-magnetic minerals in the reservoir that are too large to be transported (Wilkin and Barnes, 1997; Lin et al., 2016).

The drop in remanence at ~37 K on the cycling cooling curve in oil sample 21/24-02 (Fig. 5b) is typically indicative of monoclinic pyrrhotite, but the ZFC and FC curves (insert in Fig. 4b) do not support this argument (Kind et al., 2013). Additionally, monoclinic pyrrhotite was not observed under the SEM in any of the measured core samples. It is usually considered to be detrital in origin as it is

thought to grow too slowly in sediments to be a diagenetic product (Roberts, 2015; Horng and Roberts, 2018). Monoclinic pyrrhotite is therefore unlikely to be the cause of the reduction in remanence observed at around 37 K in oil sample 21/24-02 (RTSIRM cooling curve in Fig. 5b). It is unclear which mineral is responsible for this.

Surprisingly there was no evidence for siderite in any of the measurements from the two oil samples (Fig. 5) even though it was found in the core samples e.g. s63599 (Fig. 7j). Siderite is typically authigenic in origin and has been observed in hydrocarbon reducing environments (Burton et al., 1993; Machel, 1995; Emmerton et al., 2012; Roberts, 2015). It is possible that siderite is precipitated in the reservoir and the grains are bigger than the minimum pore throat of sandstone (2μm) or it acts as a cementing agent (Nealson, 2009; Roberts, 2015). Therefore, it is not extracted along with the oil.

5.2 Are the magnetic minerals authigenic, detrital or do they migrate?

Abubakar et al. (2015) showed that magnetic minerals are formed in situ in a mature source rock. They concluded that the vast majority of these minerals were < 60 nm and have the potential to be transported, though this may have been a result of the length of the duration lab experiments; in nature the minerals might be larger.

The magnetic minerals in the core samples are likely a mixture of authigenic, detrital and transported from source rock (Kimmeridge Clay) minerals. It is difficult to determine which of these categories the magnetic minerals in the core samples belong to. The source rock in this area is a mudstone (Kimmeridge Clay), which typically has pore throats sizes ranging from 5 nm to 100 nm while the sandstone reservoir typically has 2- 20 μm pore throat sizes (Nealson, 2009). Magnetic minerals that migrate with the oil from the source rock must be less than 100 nm as the oil also passes through layers of shale. This suggests that the < 100 nm grains which are responsible for the SP and SD FORC signatures observed in our samples, e.g. s63596, s72396 and s72403 (Figs. 7f, Figs. 8 c and l) could have been transported from the source rock while the > 150 nm grains are either detrital or authigenic. The framboids, pyrite and siderite are authigenic, while the > 1 μm magnetite grains and titanohematite are most likely detrital or as a result of drilling mud contamination. Similar observations have been made by Liu et al. (2006).

There is also the possibility that the measured magnetic response is due to chemical alteration of Fe-rich phases during the 20-30 years the cores have been stored, however, we deem this unlikely as the enhanced response is seen in several wells in multiple samples.

5.3 Unravelling the magnetic signature: End-member analysis.

For two of the wells in the area, the FORC diagrams were analysed using principal-component analysis (PCA) to help understand variance in FORC distributions as a function of depth and to help identify possible end-members (EM) (Harrison et al. (2018). To do this we used version 3.06 of the FORCinel software package (Harrison and Feinberg, 2008).

Ten samples from well 21/25-04 (Figure 7) were selected for FORC-PCA, and 95% of the variance was defined by two EMs. EM1 accounted for 90% of the variance while EM2 accounts for 5% of the variance. The data are plotted in the principal component plane in Figure 10a. The two components identified (Figs. 10c and b) are represented by SP particles (EM1) and SD particles with multi-axial anisotropy or vortex behaviour (EM2). PSD behaviour is observed in both EMs. The depth variation of the two components identified is shown in Figure 10 d. FORC-PCA for well 21/25-04 (Figure 10d) showed a noticeable increase in the proportion of SD particles (EM2) at the GOC and OWC. This is also accompanied by a reduction in the proportion of SP particles (EM1) at the GOC and an increase in proportion of EM1 at the OWC.

A new FORC-PCA was carried out on 12 samples in well 21/25-A1, and the variance in the data was defined by three newly defined EMs (Fig. 11 a). EM1 accounts of 50% of the variance while EM2 accounts for 45% and EM3 accounts for 2%. The three components identified (Fig. 11 b-d) are represented by SP particles (EM1), SP particles with multi-axial anisotropy or vortex behaviour (EM2) and stable SD greigite particles (EM3). The proportions of these end members are shown in Figure 11e. Peaks in the proportions of EM3 are found at the OWC and GOC (Fig, 11 e). The proportion of EM1 and EM2 decreases at the OWC. At the GOC, a drop in EM1 is accompanied by an increase in EM2. EM1 is more prominent below the GOC and OWC.

These SD grains identified at the hydrocarbon contacts can either be magnetite as seen in well 21/25-04 (EM2, Fig. 10) or greigite as seen in well 21/25-A1 (EM3, Fig.11). FORC-PCA aids in the

interpretation of the data as it was able to pick out trends that go unnoticed in FORC diagrams if they were just compared by mere observation. For example, the FORC diagram at the GOC for well 21/25/A1 showed no SD signal (Fig. 8f) but the PCA was able to identify a relative increase in SD particle proportions at the GOC (Fig. 11). The proportion of these SD particles is roughly correlated with the M_s, M_{rs} and susceptibility; the highest M_s, M_{rs} and susceptibility values are noticed at the GOC in well 21/25-04 (Figure 6b and e). This also corresponds to the maximum proportion of SD particles (Fig. 10 d) and is consistent with the highest M_s, M_{rs} and susceptibility values measured at the OWC in well 21/25-A1 (Figs. 6a and d) again showing the highest SD proportions (Fig. 11e).

5.4 Magnetic enhancement at the hydrocarbon-fluid contacts

FORC-PCA demonstrated the increased abundance of stable SD material at the GOC and OWC (Fig. 10d and Fig 11e). This increased abundance of larger SD grains at the hydrocarbon fluid contacts is most likely due to changes in diagenetic conditions. Here we discuss two possible mechanisms for the enhancement: (1) thermodynamic, and (2) biological.

(1) A thermodyanamic model: Burton et al. (1993) calculated thermodynamic stability diagrams for iron bearing minerals at temperatures (50- 200 ^{o}C) and pressures (1-600 bar) similar to those expected in our reservoirs. All the minerals identified in our samples are represented in the thermodynamic stability diagrams of Burton et al. (1993) apart from greigite (Figure 8l); at the time the importance of greigite was not appreciated, and was not included in their models. It is now thought, that the conditions in the reservoir can ensure the stability of greigite: A high concentration of reactive iron along with a low supply of organic carbon is needed to preserve greigite (Kao et al., 2004). Wells 21/25-04 and 21/25-A1 have API (American Petroleum Institute) gravity ranging from 40^{o} to 38^{o} API, which is indicative of sweet crude oil with low sulphur content, and has been argued to prevent greigite from altering to pyrite (Wenger et al., 2002). We suggest the thermodynamic stability diagrams in the reservoir includes a region for greigite between the pyrrhotite and pyrite regions (Sack and Ebel, 2006).

It is possible that subtle diagenetic changes in total dissolved sulphur, total dissolved iron or total dissolved inorganic carbon at the top of the oil column and at the oil-water interface could favour the precipitation of SD greigite or magnetite at the hydrocarbon contacts. A model for the formation of

magnetic minerals in the reservoir is shown in Fig. 12. SD grains are likely precipitated at the top of the oil column during early reservoir filling (Fig. 12a). This continues until the spill point is reached and a stable OWC is formed, which kick starts the formation of SD grains at the OWC (Fig. 12b). This continues as long as the trapping mechanism is unperturbed by geological processes, e.g., regional tilting, halokinesis or compression. The reservoir receives a gas charge, the gas initially dissolves in the oil and the precipitation of SD grains continues at the top of the oil column and at the OWC (Fig. 12c). A change in pressure, temperature or late gas charge results in the formation of a gas cap which displaces the oil and pushes the SD grains down the accumulation resulting in a concentration of SD grains at the GOC (Fig. 12 d).

(2) Biological mechanism: Biodegradation may be responsible for the precipitation of SD magnetic minerals at the hydrocarbon contacts. Biodegradation of hydrocarbons can occur during early reservoir filling or at the oil water interface in temperatures less than 80 ^{o}C (Head et al., 2003). Depending on the bacteria, SD magnetite or greigite may be produced. Bacteria such as GS-15 can produce fine grained extracellular magnetite via oxidation of certain hydrocarbons in an anaerobic environment while sulphate reducing bacteria such as prokaryotes generate high concentrations of hydrogen sulphide (H_2S) which combines with iron to produce fine grained greigite (Sparks et al., 1990). Wells 21/25-04 and 21/25-A1 are interpreted to have been cooler than 80 ^{o} at the onset of reservoir filling before rapid burial caused an increase in temperature (Badejo et al., 2020). It is possible that limited biodegradation would have occurred at the top of the oil column during trap filling and at the OWC resulting in precipitation of SD magnetite or greigite at the contacts prior to burial.

A schematic showing the variation of grain sizes of magnetic minerals precipitated due to the diagenetic environment caused by hydrocarbons is shown in Fig. 13. This observation could be used to identify both the OWC and GOC when conventional methods are unreliable. Given most of the magnetic minerals should remain in the host rock after hydrocarbon leakage, so this technique has the potential to identify paleo-hydrocarbon contacts; either flat or tilted due to structuration. Identification of paleo-hydrocarbon contacts can provide information on the filling history of a series of fields within a basin which can help calibrate petroleum systems models.

6. Conclusions

Peaks in measured magnetic susceptibility, saturation magnetisation and saturation remanent magnetisation values have been observed at both the GOC and OWC in Tay Formation oil fields (Fig. 6). Detailed magnetic analysis showed these peaks to be due to an increase in the proportion of single domain magnetite or greigite at the hydrocarbon fluid contacts (Figs. 10, 11 and 13). Subtle diagenetic changes at the top of the oil column and at the oil water interface are likely to be responsible for the observed anomalies at the GOC and OWC (Fig. 12). Biodegradation during early filling of the reservoir and at the OWC may also be the direct cause of or enhancement of the signal at the hydrocarbon fluid contacts. Our understanding of the processes at contacts are currently being refined as part of a new study at Imperial. This observation is of importance to the oil industry, as the presence of paleo- hydrocarbon fluid contacts can be identified by carrying out quick magnetic susceptibility measurements on whole core samples from dry wells. This would give information on the filling history of a basin, for example, through identifying a palaeo-OWC, or could be used in the calibration of petroleum systems models in both frontier and mature basins. This new method can importantly be used on core samples from hydrocarbon wells where conventional methods failed to identify the GOC or OWC.

7. Acknowledgements

This work was partly funded by Petroleum Technology Development Fund (PTDF) Nigeria, and a Visiting Fellowship to the Institute of Rock Magnetism (IRM), University of Minnesota. The IRM is funded by the Instruments and Facilities program of the Earth Sciences Division of the National Science Foundation, and by the University of Minnesota. We thank Dana Petroleum for provision of the oil samples.

401 **References**

402

403 Abubakar, R., Muxworthy, A. R., Sephton, M. A., Southern, P., Watson, J. S., Fraser, A. J., and
404 Almeida, T. P., 2015, Formation of magnetic minerals in hydrocarbon-generation conditions:
405 Marine and Petroleum Geology, v. 68, Part A, p. 509-519.

406 Abubakar, R., Muxworthy, A. R., Fraser, A., Sephton, M. A., Watson, J. S., Heslop, D., Paterson,
407 G. A., and Southern, P., 2020, Mapping hydrocarbon charge-points in the Wessex Basin
408 using seismic, geochemistry and mineral magnetics: Marine and Petroleum Geology, v.
409 111, p. 510-528.

410 Ahmed, T. H., 1989, Hydrocarbon phase behavior, Gulf Pub. Co., Houston, 424 p.

411 Aldana, M., Costanzo-Alvarez, V., and Díaz, M., 2003, Magnetic and mineralogical studies to
412 characterize oil reservoirs in Venezuela: The Leading Edge, v. 22, p. 526-529.

413 Badejo, S., Fraser, A. J., Neumaier, M., and Muxworthy, A. R., 2020, 3D Petroleum Systems
414 Modelling as an exploration tool in mature basins: A case study from the Central North Sea,
415 UK: Marine and Petroleum Geology, submitted.

416 Besnus, M., and Meyer, A., Nouvelles données expérimentales sur le magnétisme de la pyrrhotine
417 naturelle, *in* Proceedings Proc. Int. Conf. Mag, Nottingham, 1964, v. 20, p. 507-511.

418 Burton, E. A., H. G. Machel, and J. Qi, 1993, Thermodynamic constrain on anomalous
419 magnetization in shallow and deep hydrocarbon seepape environments: Society for
420 Sedimentary Geology, v. 49, p. 193-207.

421 Cayley, G., 1987, Hydrocarbon migration in the central North Sea: *in* In: Brooks, J. and Glennie, K.,
422 eds., Petroleum geology of north west Europe: Graham and Trotman, London, p. 549-555.

423 Chang, L., Roberts, A. P., Tang, Y., Rainford, B. D., Muxworthy, A. R., and Chen, Q., 2008,
424 Fundamental magnetic parameters from pure synthetic greigite (Fe3S4): Journal of
425 Geophysical Research: Solid Earth, v. 113, p. 1-16.

426 Costanzo-Alvarez, V., Aldana, M., Aristeguieta, O., Marcano, M. C., and Aconcha, E., 2000, Study
427 of magnetic contrasts in the Guafita oil field (south-western Venezuela): Physics and
428 Chemistry of the Earth, Part A: Solid Earth and Geodesy, v. 25, p. 437-445.

Dekkers, M. J., H. F. Passier, and M. A. A. Schoonen, 2000, Magnetic properties of hydrothermally synthesized greigite (F3S4) - II. High- and low-temperature characteristics: Geophysical Journal International, v. 141, p. 809-819.

Dennis, H., Baillie, J., Holt, T., and Wessel-Berg, D., 2000, Hydrodynamic activity and tilted oil-water contacts in the North Sea: Norwegian Petroleum Society Special Publications, v. 9, p. 171-185.

Dunlop, D. J., and Özdemir, Ö., 1997, Rock Magnetism: Fundamentals and Frontiers, Cambridge, Cambridge University Press, Cambridge, 573 p.

Egli, R., 2013, VARIFORC: An optimized protocol for calculating non-regular first-order reversal curve (FORC) diagrams: Global and Planetary Change, v. 110, p. 302-320.

Emmerton, S., Muxworthy, A. R., and Sephton, M. A., 2012, Magnetic characterization of oil sands at Osmington Mills and Mupe Bay, Wessex Basin, UK, *in* Elmore, D., Muxworthy, A. R., Mena, M., and Maldana, M., eds., Remagnetization and chemical alteration of sedimentary rocks, Volume 371: Geological Society, London, Special Publications, p. 189-198.

Erratt, D., Thomas, G. M., and Wall, G. R. T., 1999, The evolution of the Central North Sea Rift: Geological Society, London, Petroleum Geology Conference series, v. 5, p. 63-82.

Frederichs, T., von Dobeneck, T., Bleil, U., and Dekkers, M. J., 2003, Towards the identification of siderite, rhodochrosite, and vivianite in sediments by their low-temperature magnetic properties: Physics and Chemistry of the Earth, Parts A/B/C, v. 28, p. 669-679.

Harrison, R. J., and Feinberg, J. M., 2008, FORCinel: An improved algorithm for calculating first-order reversal curve distributions using locally weighted regression smoothing: Geochemistry, Geophysics, Geosystems, v. 9, p. 1-11.

Harrison, R. J., Muraszko, J., Heslop, D., Lascu, I., Muxworthy, A. R., and Roberts, A. P., 2018, An Improved Algorithm for Unmixing First-Order Reversal Curve Diagrams Using Principal Component Analysis: Geochemistry, Geophysics, Geosystems, v. 19, p. 1595-1610.

Head, I. M., Jones, D. M., and Larter, S. R., 2003, Biological activity in the deep subsurface and the origin of heavy oil: Nature, v. 426, p. 344.

456 Horng, C.-S., 2018, Unusual magnetic properties of sedimentary pyrrhotite in methane seepage
457 sediments: comparison with metamorphic pyrrhotite and sedimentary greigite: Journal of
458 Geophysical Research: Solid Earth, no. 123, p. 4601-4617.
459 Horng, C. S., and Roberts, A. P., 2018, The low-temperature Besnus magnetic transition: signals
460 due to monoclinic and hexagonal pyrrhotite: Geochemistry Geophysics Geosystems, v. 19,
461 p. 3364-3375.
462 Housen, B. A., Banerjee, S. K., and Moskowitz, B. M., 1996, Low-temperature magnetic properties
463 of siderite and magnetite in marine sediments: Geophysical Research Letters, v. 23, p.
464 2843-2846.
465 Isaksen, G. H., 2004, Central North Sea hydrocarbon systems: Generation, migration, entrapment,
466 and thermal degradation of oil and gas: AAPG bulletin, v. 88, p. 1545-1572.
467 Kao, S.-J., Horng, C.-S., Roberts, A. P., and Liu, K.-K., 2004, Carbon–sulfur–iron relationships in
468 sedimentary rocks from southwestern Taiwan: influence of geochemical environment on
469 greigite and pyrrhotite formation: Chemical Geology, v. 203, p. 153-168.
470 Kind, J., Gehring, A. U., García-Rubio, I., Charilaou, M., Nowaczyk, N. R., and Löffler, J. F., 2013,
471 Domain-wall dynamics in 4C pyrrhotite at low temperature: Geophysical Journal
472 International, v. 195, p. 192-199.
473 Kubala, M., Bastow, M., Thompson, S., Scotchman, I., and Oygard, K., 2003, Geothermal regime,
474 petroleum generation and migration, *in* Evans, D, Graham, C, Armour, A, and Bathurst, P.,
475 eds., The Millennium Atlas: Petroleum Geology of the Central and Northern North Sea, The
476 Geological Society of London, London, p. 289-215.
477 Larter, S., and di Primio, R., 2005, Effects of biodegradation on oil and gas field PVT properties
478 and the origin of oil rimmed gas accumulations: Organic Geochemistry, v. 36, p. 299-310.
479 Lascu, I., Einsle, J. F., Ball, M. R., and Harrison, R. J., 2018, The vortex state in geologic materials:
480 A micromagnetic perspective: Journal of Geophysical Research: Solid Earth, no. 123, p. 1-
481 20.
482 Lin, Q., Wang, J., Algeo, T. J., Sun, F., and Lin, R., 2016, Enhanced framboidal pyrite formation
483 related to anaerobic oxidation of methane in the sulfate-methane transition zone of the
484 northern South China Sea: Marine Geology, v. 379, p. 100-108.

485 Liu, Q., Liu, Q., Chan, L., Yang, T., Xia, X., and Cheng, T., 2006, Magnetic enhancement caused
486 by hydrocarbon migration in the Mawangmiao Oil Field, Jianghan Basin, China: Journal of
487 Petroleum Science and Engineering, v. 53, p. 25-33.
488 Machel, H. G., 1995, Magnetic mineral assemblages and magnetic contrasts in diagenetic
489 environments – with implications for studies of palaeomagnetism, hydrocarbon migration
490 and exploration, *in* Turner, P., and Turner, A., eds., Palaeomagnetic Applications in
491 Hydrocarbon Exploration and Production, Volume 98: London, Geology Society Special
492 Publications, p. 9-29.
493 Sparks, N., Mann, S., Frankel, R. B., Bazylinski, D. A., and Jannasch, H. W., 1990,
494 Biomineralization of ferrimagnetic greigite (Fe3S4) and iron pyrite (FeS2) in a magnetotactic
495 bacterium: Nature, v. 343, p. 258-261.
496 Mena, M., and Walther, A. M., 2012, Rock magnetic properties of drill cutting from a hydrocarbon
497 exploratory well and their relationship to hydrocarbon presence and petrophysical
498 properties: Geological Society, London, Special Publications, v. 371, p. 217-228.
499 Morin, F. J., 1950, Magnetic susceptibility of αFe2O3 and αFe2O3 with added titanium: Physical
500 Review, v. 78, p. 819-820.
501 Muxworthy, A. R., 2001, Effect of grain interactions on the frequency dependence of magnetic
502 susceptibility: Geophysical Journal International, v. 144, p. 441-447.
503 Nealson, P. H., 2009, Pore-throat sizes in sandstones, tight sandstones, and shales: AAPG
504 Bulletin, v. 93, p. 329-340.
505 Reynolds, R. L., Fishman, N. S., Wanty, R. B., and Goldhaber, M. B., 1990, Iron sulfide minerals at
506 Cement oil field, Oklahoma: Implications for magnetic detection of oil fields: Geological
507 Society of America Bulletin, v. 102, p. 368-380.
508 Rider, M. H., and Kennedy, M., 1996, The Geological Interpretation of Well Logs, Rider-French,
509 Aberdeen, 440 p.
510 Roberts, A. P., Pike, C. R., and Verosub, K. L., 2000, First-order reversal curve diagrams: A new
511 tool for characterizing the magnetic properties of natural samples: Journal of Geophysical
512 Research: Solid Earth, v. 105, p. 28461-28475.

513 Roberts, A. P., Heslop, D., Zhao, X., and Pike, C. R., 2014, Understanding fine magnetic particle
514 systems through use of first-order reversal curve diagrams: Reviews of Geophysics, v. 52,
515 p. 557-602.
516 Roberts, A. P., 2015, Magnetic mineral diagenesis: Earth-Science Reviews, v. 151, p. 1-47.
517 Roberts, A. P., Almeida, T. P., Church, N. S., Harrison, R. J., Heslop, D., Li, Y., Li, J., Muxworthy,
518 A. R., Williams, W., and Zhao, X., 2017, Resolving the origin of pseudo-single domain
519 magnetic behavior: Journal of Geophysical Research: Solid Earth, v. 122, no. 12, p. 9534-
520 9558.
521 Roberts, A. P., Zhao, X., Harrison, R. J., Heslop, D., Muxworthy, A. R., Rowan, C. J., Larrasoaña,
522 J.-C., and Florindo, F., 2018, Signatures of reductive magnetic mineral diagenesis from
523 unmixing of first-order reversal curves: Journal of Geophysical Research: Solid Earth, v.
524 123, no. 6, p. 4500-4522.
525 Sack, R. O., and Ebel, D. S., 2006, Thermochemistry of Sulfide Mineral Solutions: Reviews in
526 Mineralogy and Geochemistry, v. 61, p. 265-364.
527 Sprain, C. J., Feinberg, J. M., Renne, P. R., and Jackson, M., 2016, Importance of titanohematite in
528 detrital remanent magnetizations of strata spanning the Cretaceous-Paleogene boundary,
529 Hell Creek region, Montana: Geochemistry, Geophysics, Geosystems, v. 17, p. 660-678.
530 Valdez-Grijalva, M. A., Muxworthy, A. R., Williams, W., Ó Conbhuí, P., Nagy, L., Roberts, A. P.,
531 and Heslop, D., 2018, Magnetic vortex effects on first-order reversal curve (FORC)
532 diagrams for greigite dispersions: Earth and Planetary Science Letters, v. 501, p. 103-111.
533 Valdez-Grijalva, M. A., and Muxworthy, A. R., 2019, First-order reversal curve (FORC) diagrams of
534 nanomagnets with cubic magnetocrystalline anisotropy: A numerical approach: Journal of
535 Magnetism and Magnetic Materials, v. 471, p. 359-364.
536 Verwey, E. J. W., 1939, Electronic conduction of magnetite (Fe3O4) and its transition point at low
537 temperatures: Nature, v. 144, p. 327-328.
538 Wenger, L. M., Davis, C. L., and Isaksen, G. H., 2002, Multiple Controls on Petroleum
539 Biodegradation and Impact on Oil Quality, v. 5, p. 375-383.
540 Wilkin, R. T., and Barnes, H. L., 1997, Formation processes of framboidal pyrite: Geochimica et
541 Cosmochimica Acta, v. 61, no. 2, p. 323-339.

542 Zhao, X., Heslop, D., and Roberts, A. P., 2015, A protocol for variable-resolution first-order reversal
543 curve measurements: Geochemistry, Geophysics, Geosystems, v. 16, p. 1364–1377.
544

Figure Captions

Figure 1. Wireline logs for well 21/25-04. GR- gamma ray log, ILD- Deep induction log used to determine formation resistivity, RHOB- density log and NPHI- neutron porosity Log. A decrease in resistivity indicates a change from hydrocarbons to formation water.

Figure 2. Study area (red rectangle) located in the Western Central Graben of the UK North Sea. Known hydrocarbon field are highlighted in green.

Figure 3. Tectonostratigraphy of the western Central Graben of the UK North Sea showing lithology and ages of rifting in the study area. Kimm clay= Kimmeridge clay, FM= formation and SM= sandstone member.

Figure 4. Cycling cooling/warming curves and FC/ZFC curves for a) pure Kaolinite clay- noisy signal, b) oil sample from well 21/24-02- cycling and warming curves suggest the presence of magnetite and possibly monoclinic pyrrhotite in the sample. c) oil sample from well 21/29a-08 - cycling cooling and warming curves suggest the presence of magnetite in the sample.

Figure 5. Hysteresis loop of sample s63654 from well 21/25-04 annotating saturation magnetisation (M_s), remanent saturation magnetisation (M_{rs}) and coercivity (H_c)

Figure 6. M_s (green line), M_{rs} (black line), susceptibility measured at 990 Hz (red line) and 6000 Hz (blue line) for samples from wells 21/25-A1 (a and d), 21/25-04 (b and e) and 21/29a-09 (c and f). Distinct peaks are noticed at the GOC (red dashed line) and OWC (blue dashed line). GOC and OWC depths were obtained from wireline logs. All depths are below mean sea level.

Figure 7. LT experiments (cycling cooling, cycling warming, FC and ZFC), HT susceptibility experiments and FORC diagrams for samples in well 21/25-04. S63594; a) LT experiments suggest the presence of titanohematite or goethite and magnetite, b) HT experiment suggests a siderite rich sample and c) FORC diagram suggests a mixture of SP grains with multi axial anisotropy or a vortex structure and PSD grains. S63596 at the GOC; d) LT experiments suggest the presence of titanohematite or goethite and magnetite, e) HT experiment suggests a siderite rich sample with some iron sulphides and f) FORC diagram suggests a mixture of SD grains with multi axial anisotropy or vortex structure and PSD grains. S63598; g) LT experiments suggest the presence of

572 titanohematite or goethite and magnetite, h) HT experiment suggests a siderite rich sample and i)
573 FORC diagram suggests a mixture of SP grains with multi axial anisotropy or a vortex structure and
574 PSD grains. S63599 at the OWC; j) LT experiments suggest the presence of hematite, siderite and
575 magnetite, k) HT experiment suggests a siderite rich sample and l) FORC diagram suggests the
576 presence of SD grains. S63600; m) LT experiments suggest the presence of titanohematite or
577 goethite and magnetite, n) HT experiment suggests a siderite rich sample and o) FORC diagram
578 suggests the presence of SP grains. VARIFORC parameter (Egli, 2013) for FORC smoothing are
579 $s_{c,0}$ = 1.2, $s_{c,1}$ = 3, $s_{b,0}$ = 3, $s_{b,1}$ = 5, and λ_c = 1 λ_b = 1. Samples were heated in argon.

580 Figure 8. LT experiments (cycling cooling, cycling warming, FC and ZFC), HT susceptibility
581 experiments and FORC diagrams for samples in well 21/25-A1. S72396; a) LT experiments suggest
582 the presence of titanohematite or goethite and magnetite, b) HT experiment suggests a siderite rich
583 sample and c) FORC diagram suggests the presence of SP grains with multi axial anisotropy or a
584 vortex structure. S72397 at the GOC; d) LT experiments suggest the presence of titanohematite or
585 goethite and magnetite, e) HT experiment suggests a mixture of siderite and iron sulphides and f)
586 FORC diagram suggests a mixture of SP and SD grains with multi axial anisotropy or vortex structure.
587 S72399; g) LT experiments suggest the presence of titanohematite or goethite, siderite and
588 magnetite, h) HT experiment suggests the presence of siderite and iron sulphides and i) FORC
589 diagram suggests the presence of SP grains with multi axial anisotropy or vortex structure. S72403
590 at the OWC; j) LT experiments suggest the presence of titanohematite or goethite and magnetite, k)
591 HT experiment suggests the presence of siderite and iron sulphides and l) FORC diagram suggests
592 the presence of SD greigite grains. S72406; m) LT experiments suggest the presence of
593 titanohematite or goethite and magnetite, n) HT experiment suggests an iron sulphide rich sample
594 and o) FORC diagram suggests the presence of SP grains. VARIFORC parameter (Egli, 2013) for
595 FORC smoothing are $s_{c,0}$ = 1.2, $s_{c,1}$ = 3, $s_{b,0}$ = 3, $s_{b,1}$ = 5, and λ_c = 1 λ_b = 1. Samples were heated in
596 argon.

597 Figure 9. SEM images on the Phenom desktop SEM a) s63597 EDX confirms FeS Framboid. SEM
598 images on the LEO SEM; b and c) s63598 from well 21/25-04, and d) s63600 from well 21/25-04.
599 Py- pyrite, M- magnetite and G- greigite.

Figure 10. FORC-PCA for well 21/25-04. a) principal-component space, b) end member 2 represents SD particles with multi axial anisotropy, c) end member 1 represents SP particles and d) proportions of EM1 and EM2 as a function of depth showing an increase in proportion of EM2 at the GOC (red dashed line) and OWC (blue dashed line). VARIFORC parameter (Egli, 2013) for FORC PCA smoothing are $s_{c,0}$ = 1.2, $s_{c,1}$ = 3, $s_{b,0}$ = 3, $s_{b,1}$ = 5, and λ_c = 1 λ_b = 1.

Figure 11 FORC-PCA for well 21/25-A1. a) principal component plane, b) end member 1- SP particles, c) end member 2- SP particles with multi axial anisotropy, d) end member 3- stable SD greigite particles and e) proportions of EM1, EM2 and EM3 as a function of depth showing an increase in proportion of EM3 at the GOC (red dashed line) and OWC (blue dashed line). VARIFORC parameter (Egli, 2013) for FORC PCA smoothing are $s_{c,0}$ = 1.2, $s_{c,1}$ = 3, $s_{b,0}$ = 3, $s_{b,1}$ = 5, and λ_c = 1 λ_b = 1.

Figure 12. A schematic detailing the formation of SD grain at the GOC and OWC: a) formation of SD grains at the top of the oil during early reservoir filling, b) oil has filled to the spill point and the precipitation of SD grains occur at a stable OWC, c) the reservoir is charged with gas which dissolves in the oil, and the OWC is still stable which results in continued precipitation of SD grains, and d) a gas cap is formed pushing the SD grains formed at the top of the oil column to the GOC.

Figure 13. A schematic of the authigenic ferromagnetic magnetic mineral grain sizes as a function of depth within the reservoir.

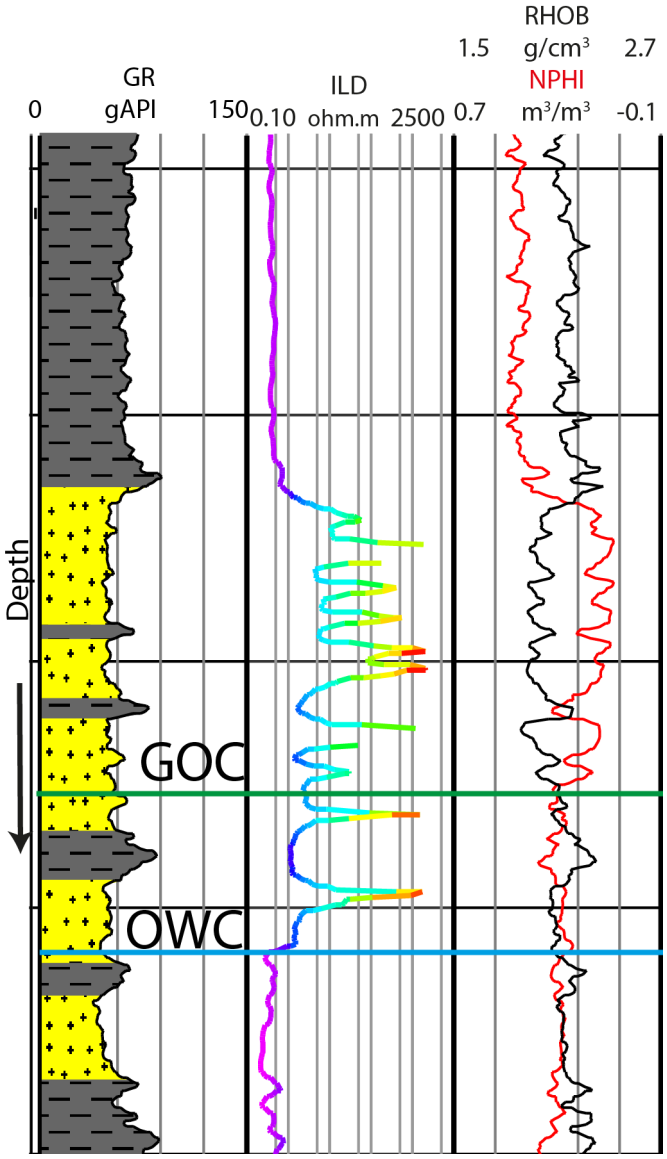

618

619 Figure 1.

620

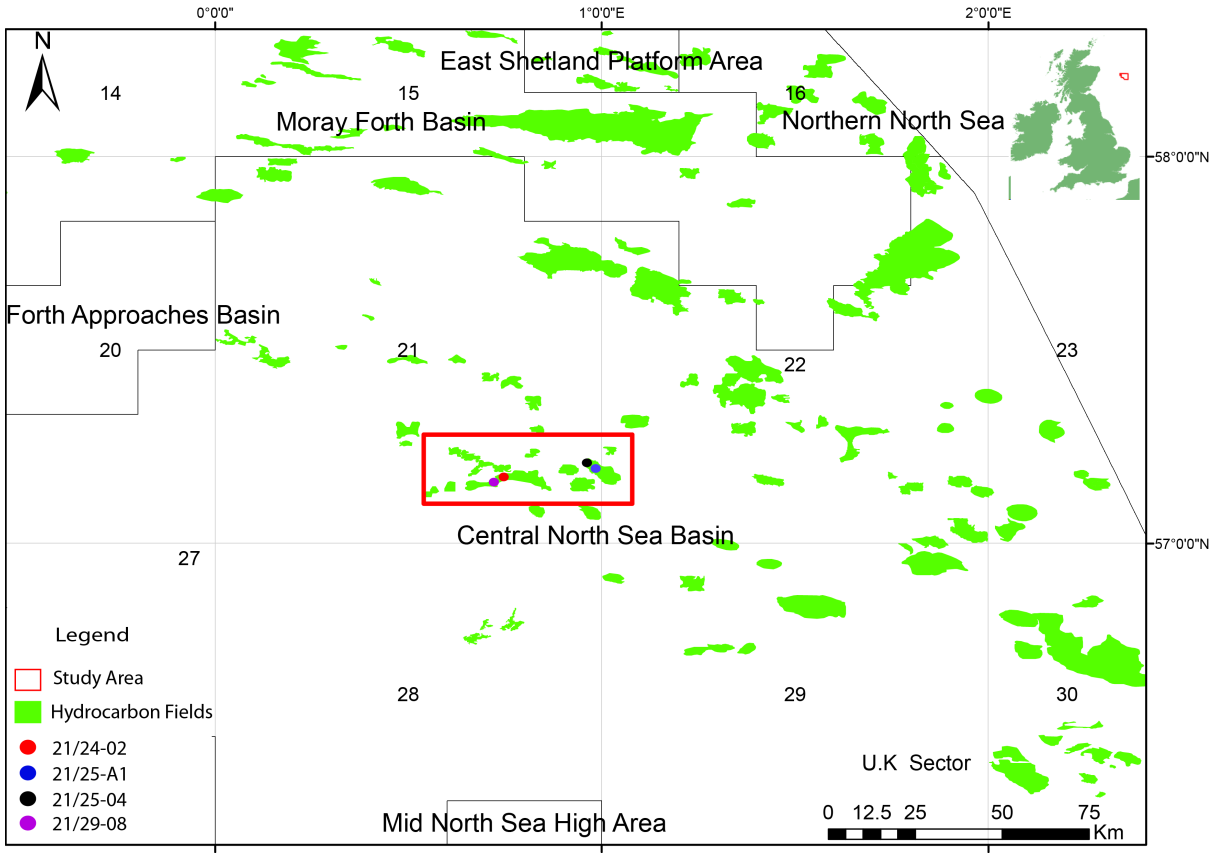
0°0'0"
1°0'0"E
2°0'0"E
N
14
15
16
East Shetland Platform Area
Moray Forth Basin
Northern North Sea
58°0'0"N
Forth Approaches Basin
20
21
22
23
Central North Sea Basin
57°0'0"N
27
Legend
Study Area
Hydrocarbon Fields
21/24-02
21/25-A1
21/25-04
21/29-08
28
29
30
U.K Sector
Mid North Sea High Area
0 12.5 25 50 75
Km

Figure 2.

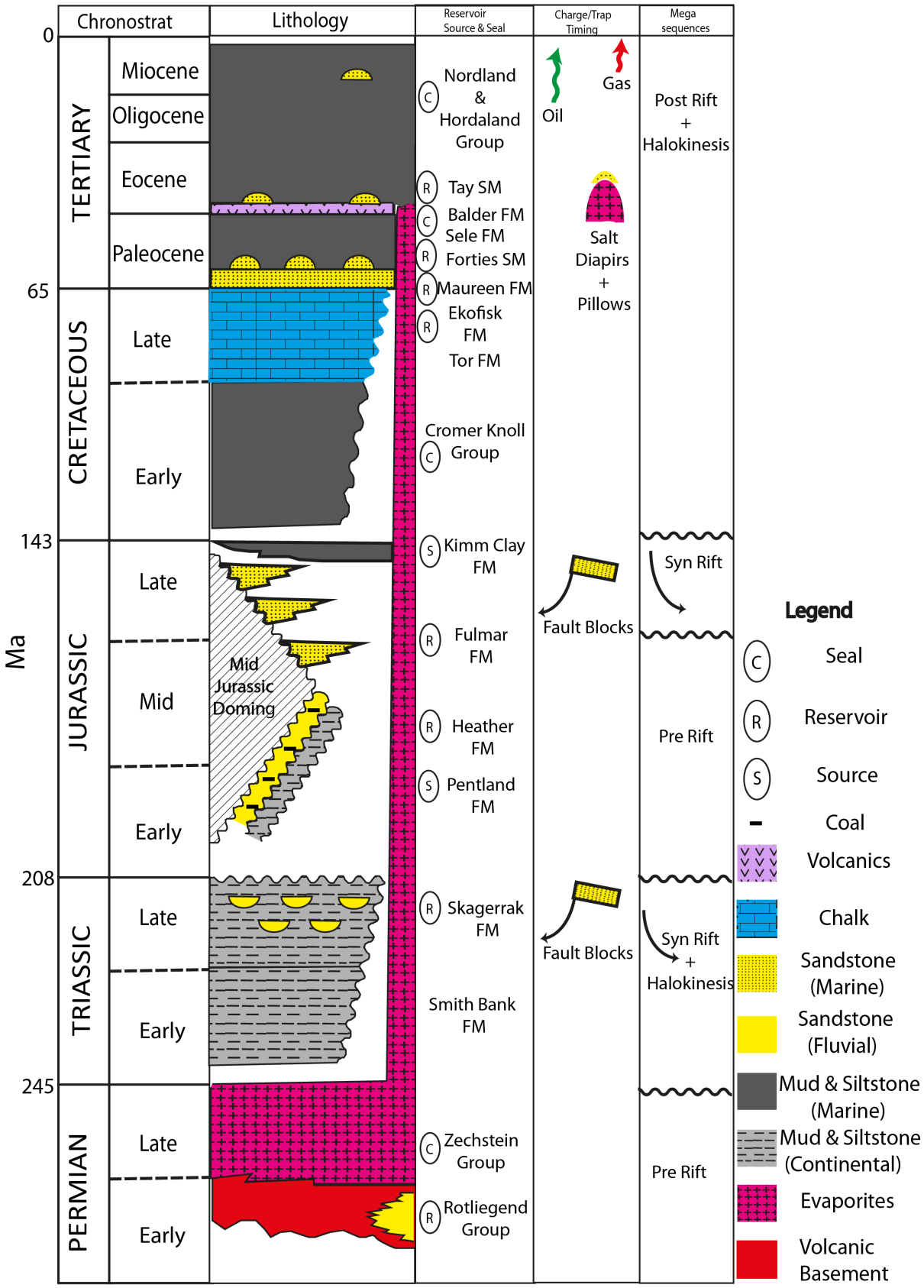
Chronostrat
Lithology
Reservoir Source & Seal
Charge/Trap Timing
Mega sequences
Ma
0
65
143
208
245
TERTIARY
Miocene
Oligocene
Eocene
Paleocene
CRETACEOUS
Late
Early
JURASSIC
Late
Mid
Early
TRIASSIC
Late
Early
PERMIAN
Late
Early
Mid Jurassic Doming
Nordland & Hordaland Group
Tay SM
Balder FM
Sele FM
Forties SM
Maureen FM
Ekofisk FM
Tor FM
Cromer Knoll Group
Kimm Clay FM
Fulmar FM
Heather FM
Pentland FM
Skagerrak FM
Smith Bank FM
Zechstein Group
Rotliegend Group
Oil
Gas
Salt Diapirs + Pillows
Fault Blocks
Fault Blocks
Post Rift + Halokinesis
Syn Rift
Pre Rift
Syn Rift + Halokinesis
Pre Rift
Legend
Seal
Reservoir
Source
Coal
Volcanics
Chalk
Sandstone (Marine)
Sandstone (Fluvial)
Mud & Siltstone (Marine)
Mud & Siltstone (Continental)
Evaporites
Volcanic Basement

Figure 3.

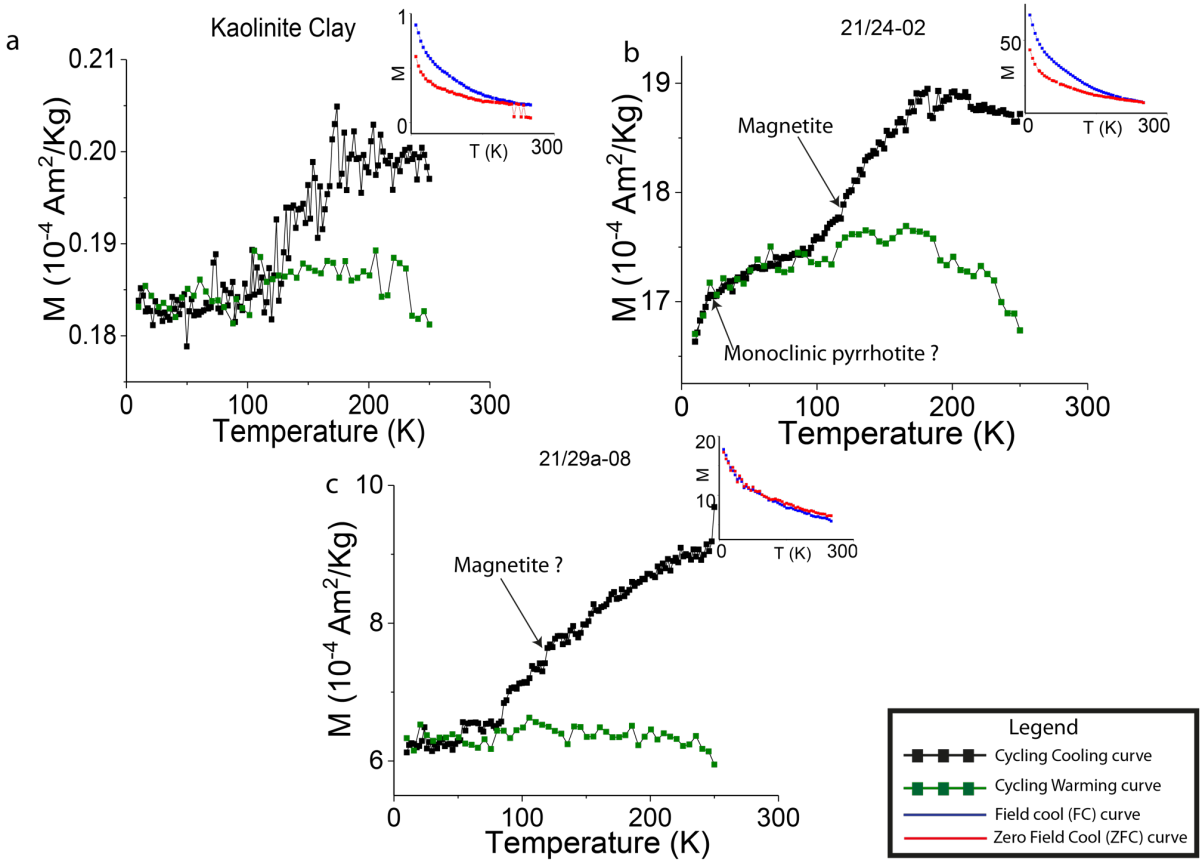

626

627 Figure 4.

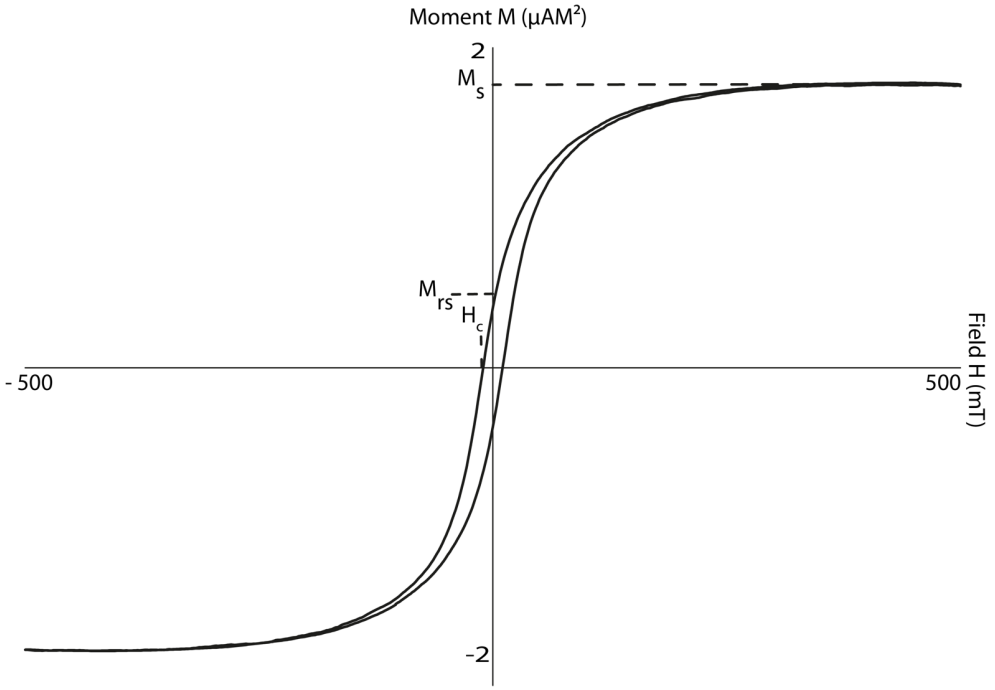

628

629 Figure 5.

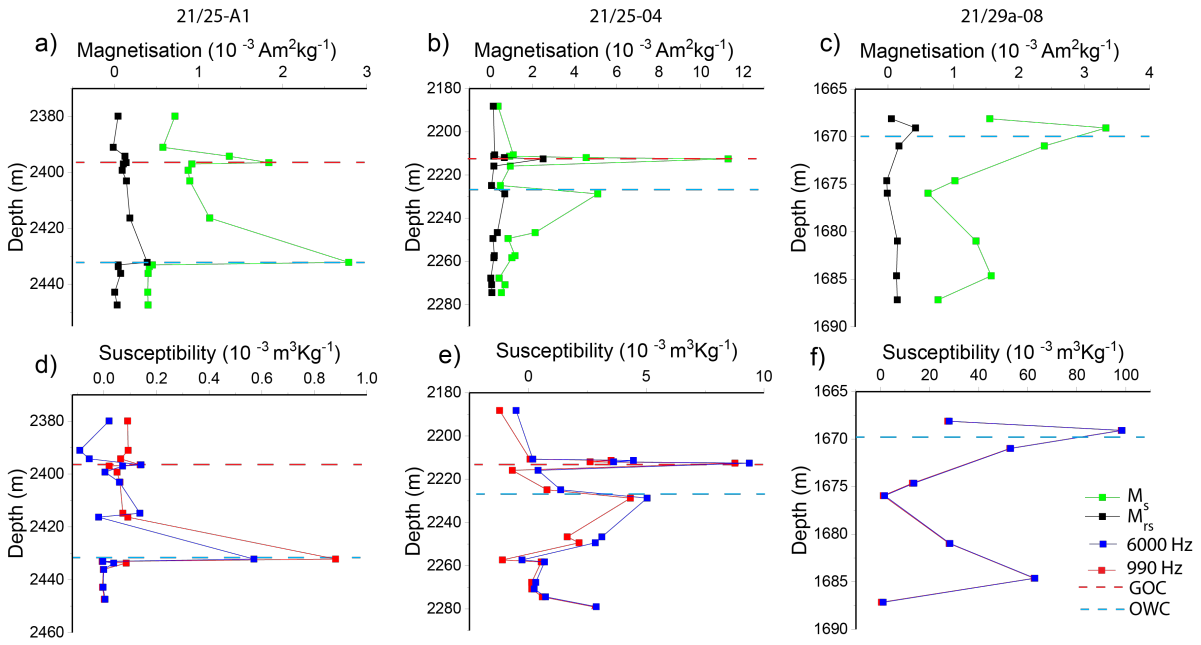
21/25-A1
21/25-04
21/29a-08
a)
b)
c)
Magnetisation (10 -3 Am2kg-1)
d)
e)
f)
Susceptibility (10 -3 m3Kg-1)
Depth (m)
Ms
Mrs
6000 Hz
990 Hz
GOC
OWC

Figure 6.

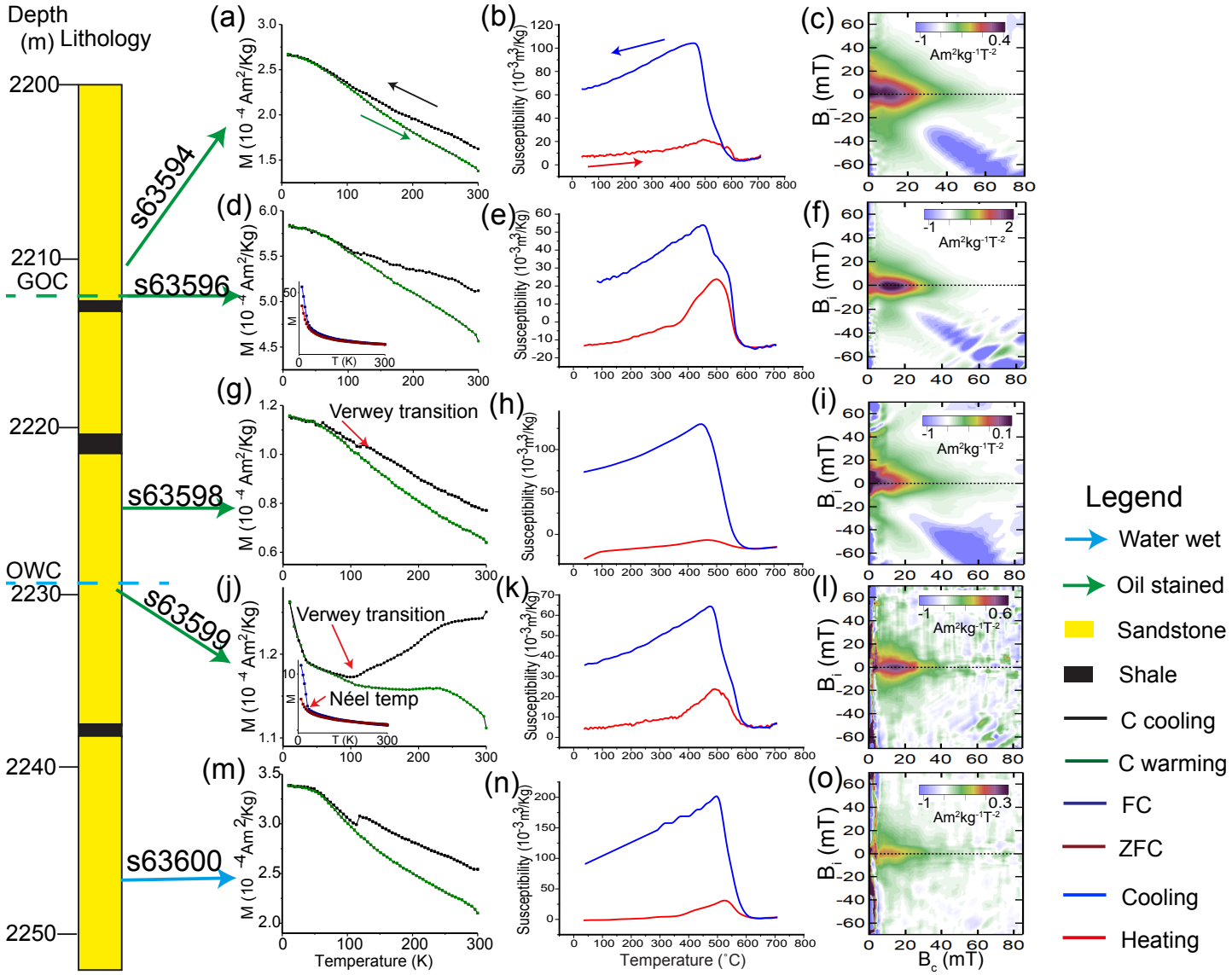
Depth
(m) Lithology
2200
2210
GOC
2220
OWC
2230
2240
2250
s63594
s63596
s63598
s63599
s63600
(a)
(b)
(c)
(d)
(e)
(f)
(g)
(h)
(i)
(j)
(k)
(l)
(m)
(n)
(o)
M (10 -4 Am2/Kg)
Susceptibility (10-3m3/Kg)
Bi (mT)
Bc (mT)
Am2kg-1T-2
Verwey transition
Néel temp
T (K)
Temperature (K)
Temperature (˚C)
Legend
Water wet
Oil stained
Sandstone
Shale
C cooling
C warming
FC
ZFC
Cooling
Heating

Figure 7.

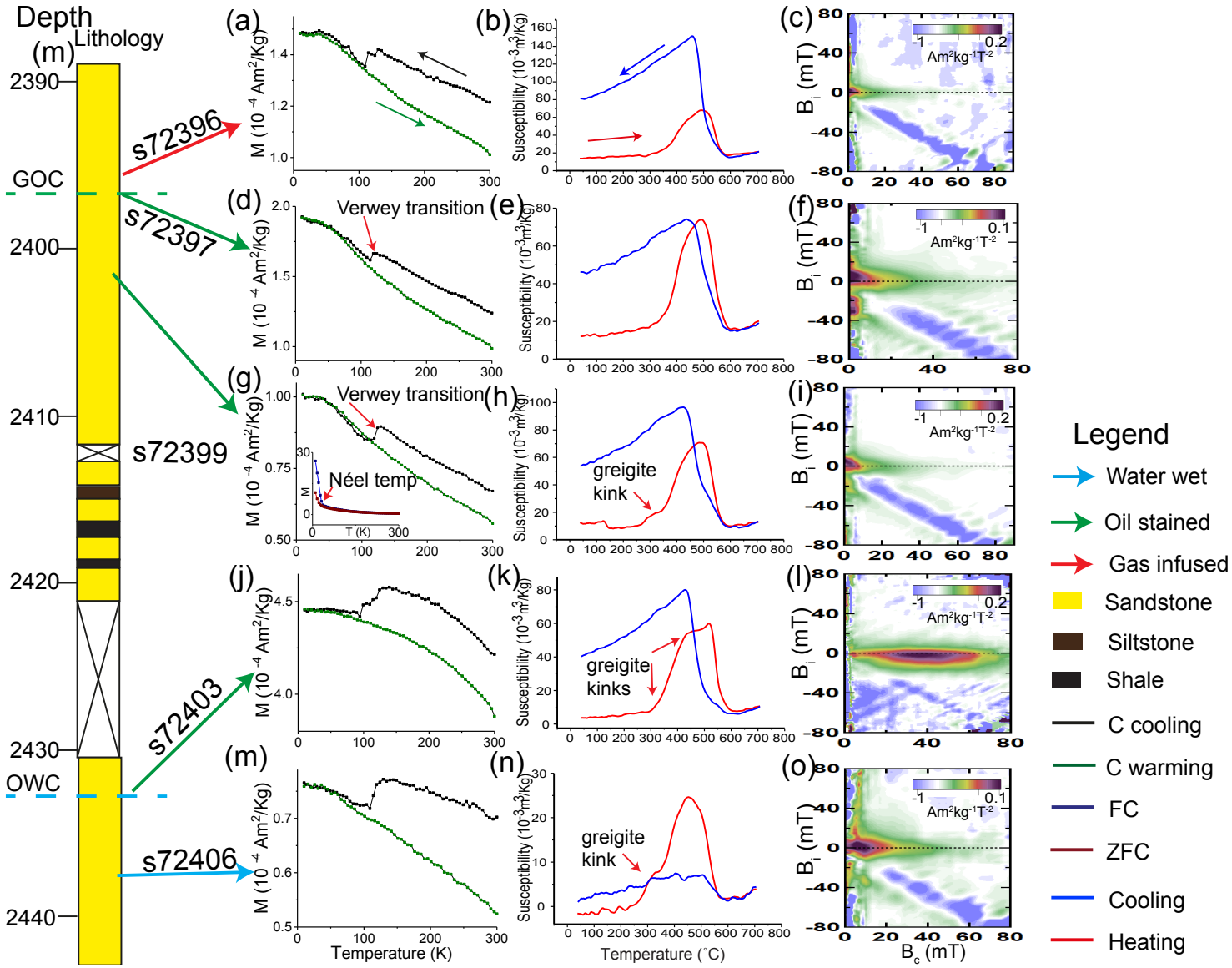
Depth
(m)
Lithology
2390
GOC
2400
2410
2420
2430
OWC
2440
s72396
s72397
s72399
s72403
s72406
(a)
(b)
(c)
(d)
(e)
(f)
(g)
(h)
(i)
(j)
(k)
(l)
(m)
(n)
(o)
Verwey transition
Néel temp
greigite kink
greigite kinks
M (10⁻⁴ Am²/Kg)
Susceptibility (10⁻³m³/Kg)
B_i (mT)
B_c (mT)
Temperature (K)
Temperature (˚C)
T (K)
Legend
Water wet
Oil stained
Gas infused
Sandstone
Siltstone
Shale
C cooling
C warming
FC
ZFC
Cooling
Heating

Figure 8.

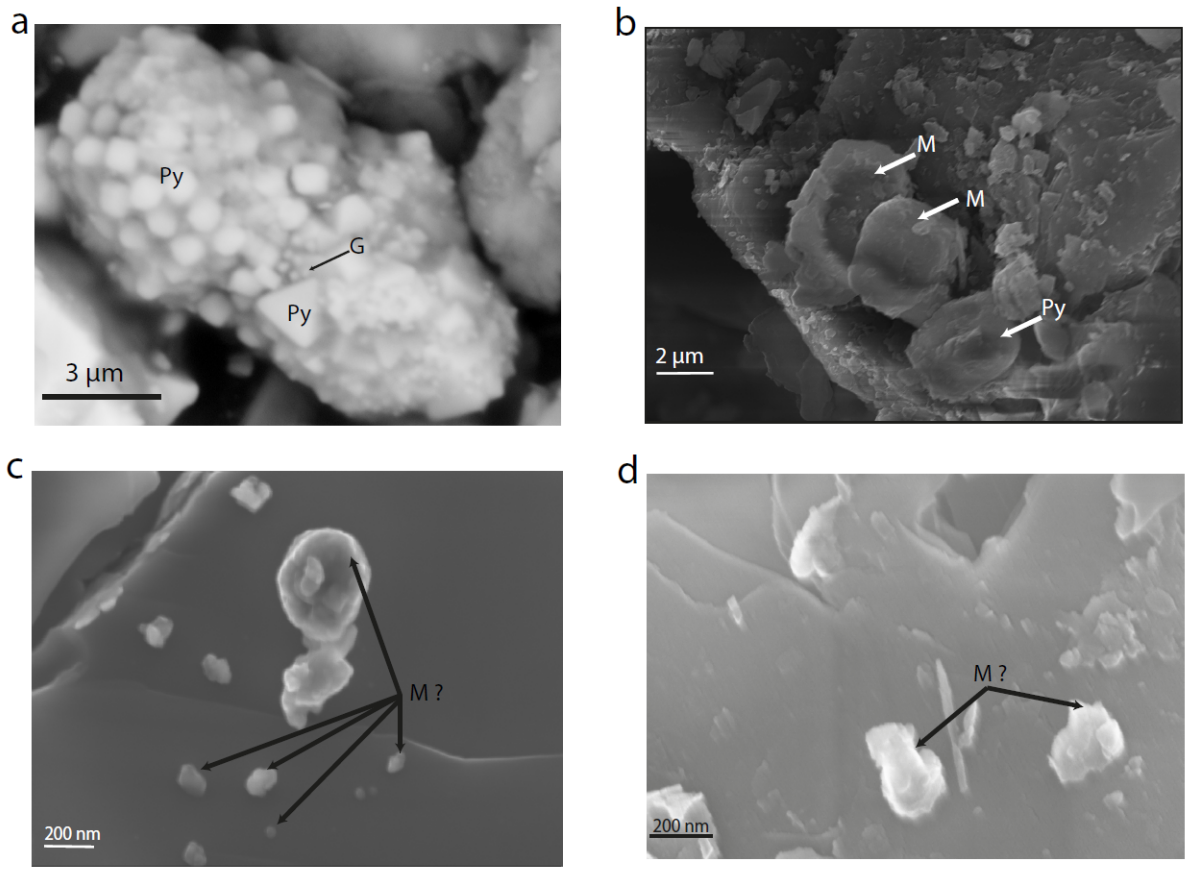

Figure 9.

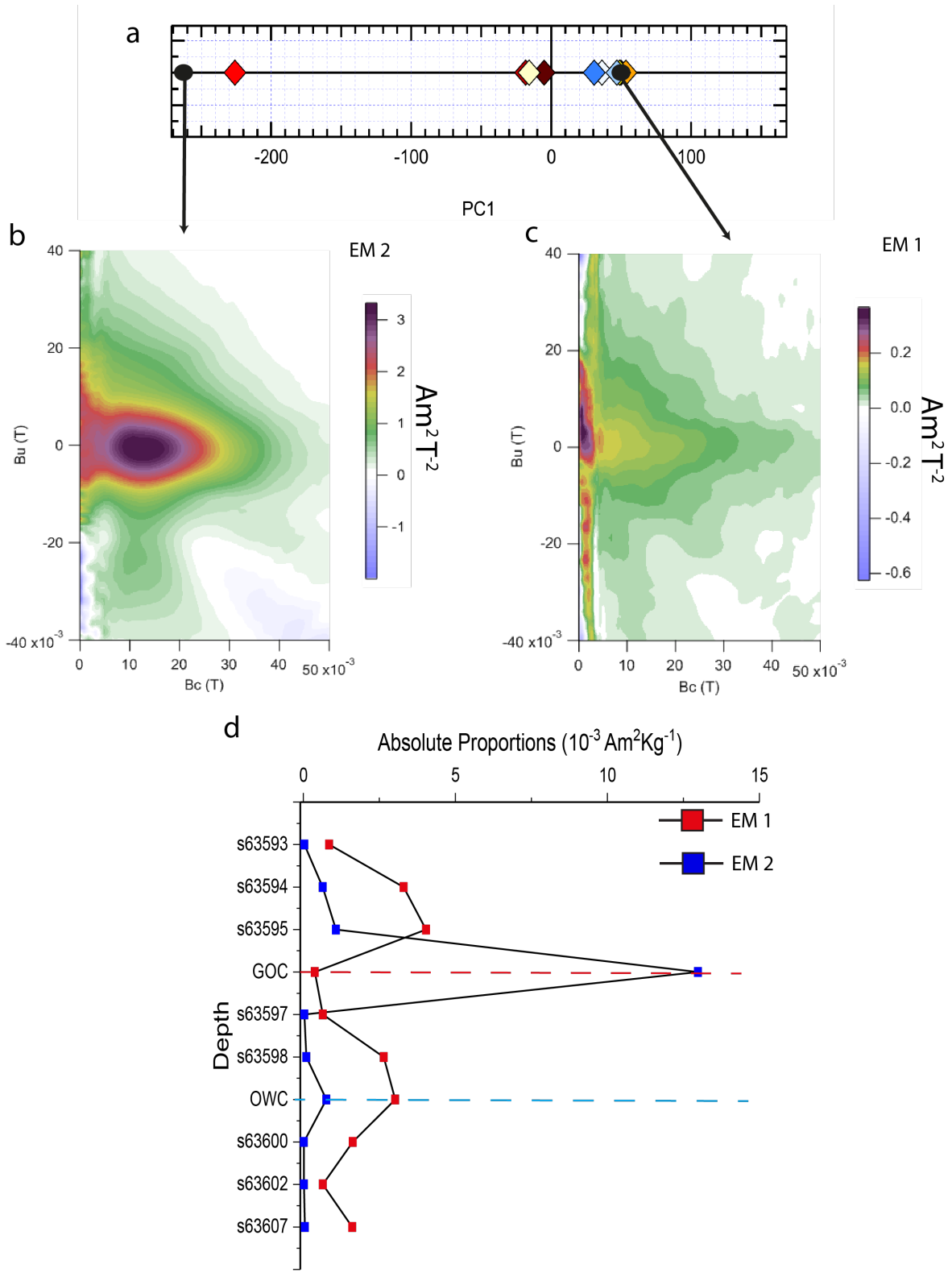
a
-200
-100
0
100
PC1
b
EM 2
40
20
0
-20
-40 x10-3
Bu (T)
0
10
20
30
40
50 x10-3
Bc (T)
3
2
1
0
-1
Am2T-2
c
EM 1
0.2
0.0
-0.2
-0.4
-0.6
d
Absolute Proportions (10-3 Am2Kg-1)
0
5
10
15
EM 1
EM 2
Depth
s63593
s63594
s63595
GOC
s63597
s63598
OWC
s63600
s63602
s63607

Figure 10

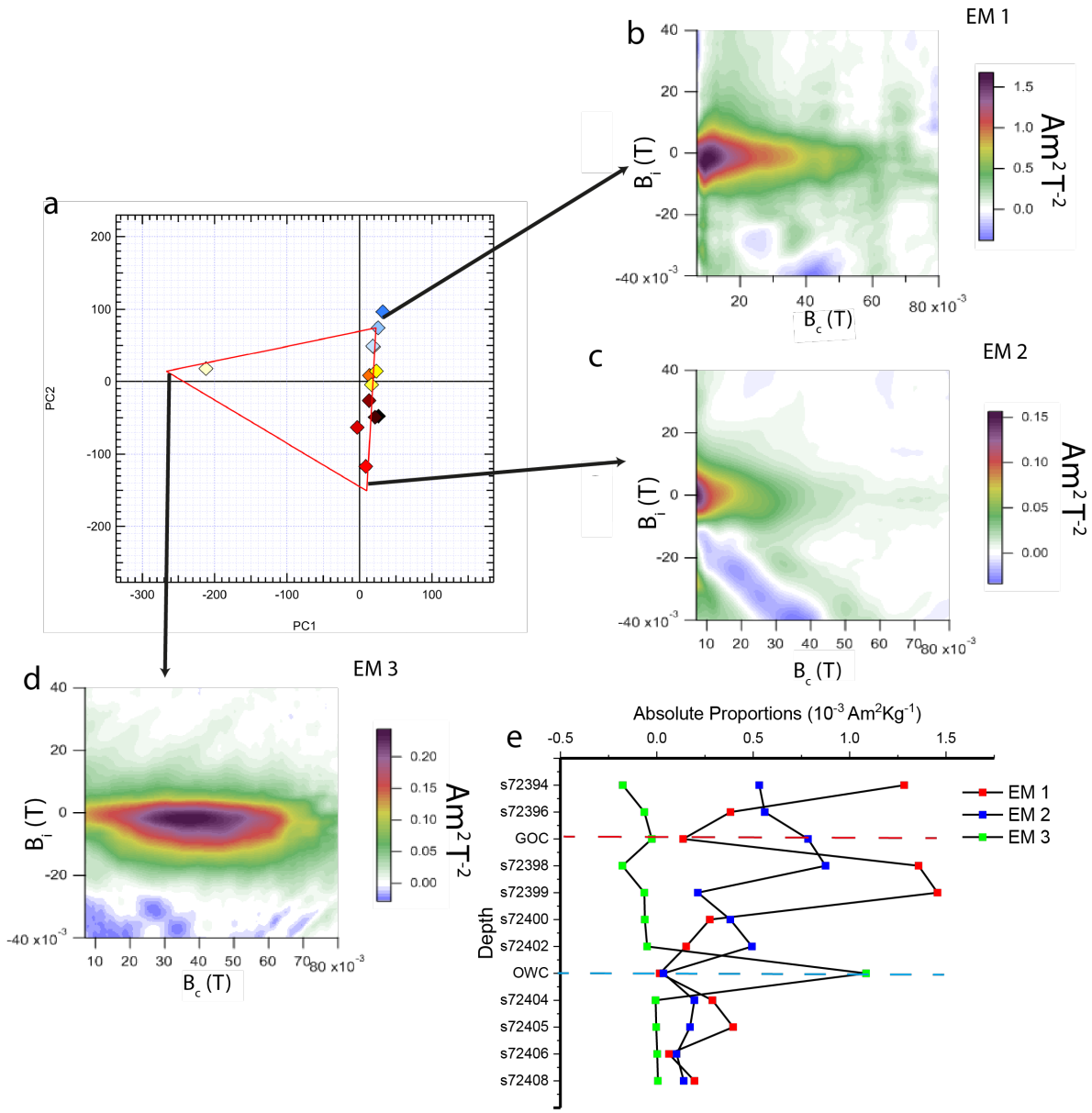
a
PC1
PC2
b
EM 1
B_i (T)
B_c (T)
Am^2T^{-2}
c
EM 2
d
EM 3
e
Absolute Proportions (10^{-3} Am^2Kg^{-1})
Depth
s72394
s72396
GOC
s72398
s72399
s72400
s72402
OWC
s72404
s72405
s72406
s72408

Figure 11

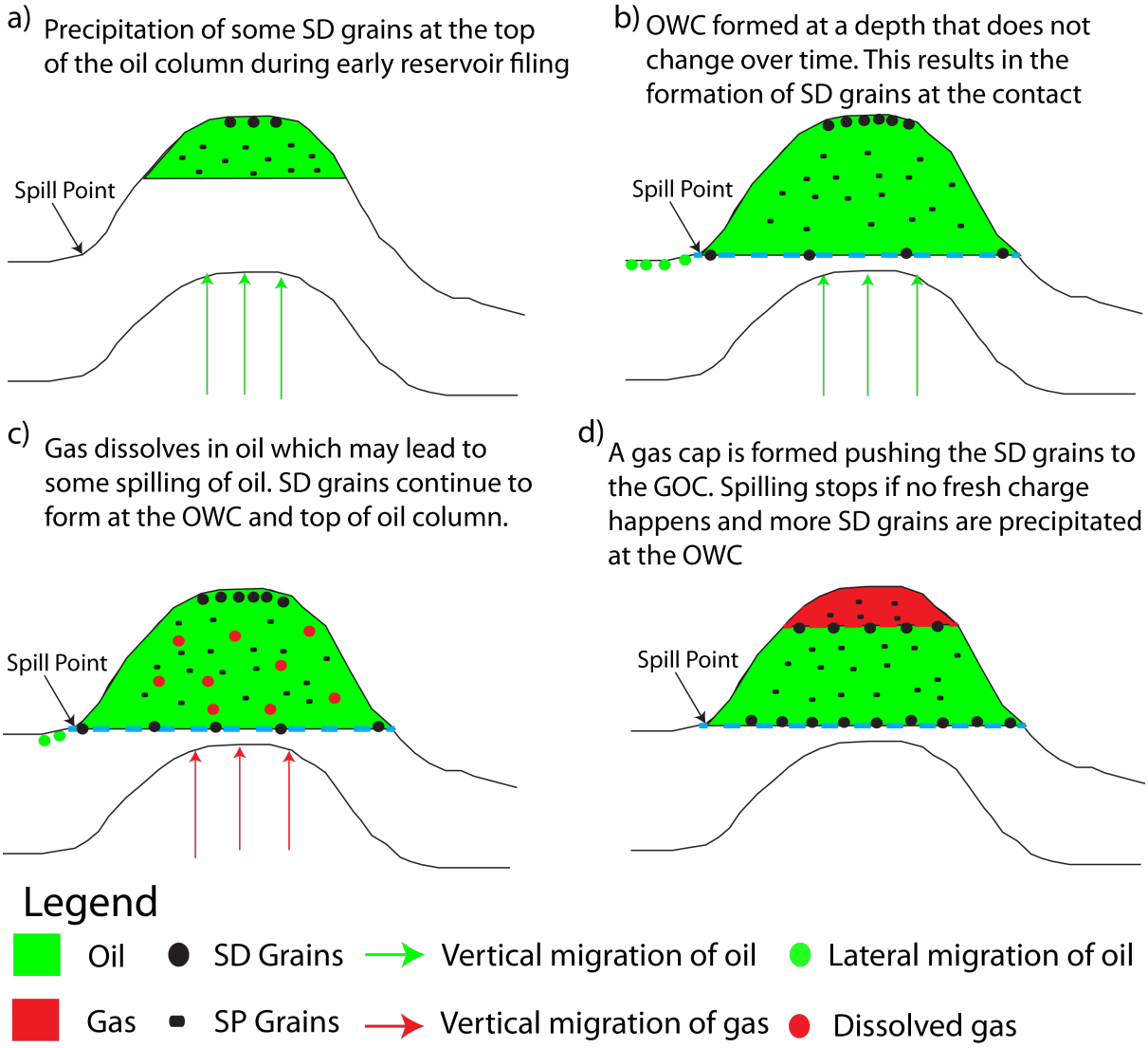

660

661 Figure 12

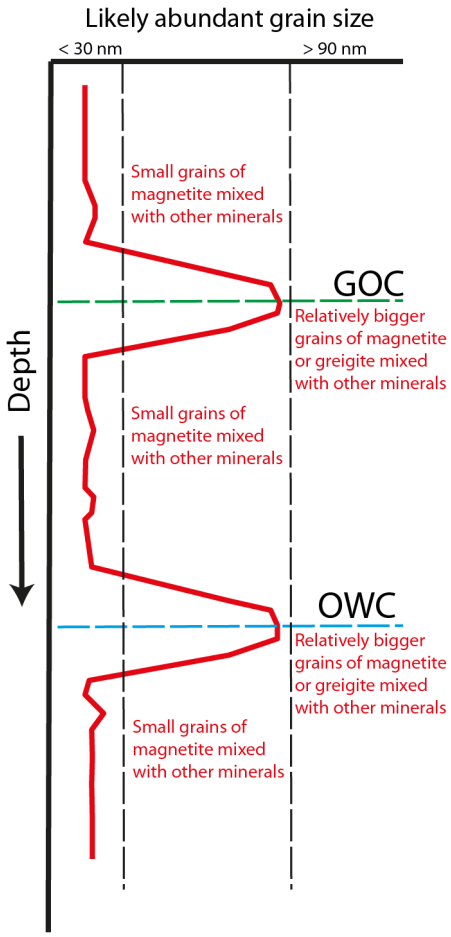

662

663 Figure 13.